
Fourier-Space, Nonlinear Rayleigh–Taylor Growth Measurements of 3-D Laser-Imprinted Modulations in Planar Targets

Introduction

The unstable growth of target nonuniformities is the most important factor that limits target performance in inertial confinement fusion (ICF)¹ and is crucial in understanding many astrophysics phenomena.² In ICF, the target is driven either directly with laser beams (direct drive)³ or indirectly by x rays, in which the laser drive is converted into x rays in a high-Z enclosure (hohlraum).⁴ When laser light is incident on the target in a direct-drive configuration, the pressure created by the target ablation launches a shock wave that compresses the target. Any target modulations, either existing surface imperfections or modulations created by laser nonuniformities through laser imprinting, grow because of shock-driven Richtmyer–Meshkov (RM) instability as a shock wave propagates toward the rear surface of the target.^{5–8} When the shock front reaches the rear surface of the target, it sends a rarefaction wave back toward the ablation surface; when it arrives, the target begins to accelerate. During the acceleration phase, the ablation-surface modulations grow exponentially because of Rayleigh–Taylor (RT) instability.^{9–19} RT instability has been extensively studied in both ablative^{12–19} and classical^{9–11} (with no ablative stabilization) regimes. RT growth rates were studied in the linear regime of the instability with both direct^{14–17} and indirect^{12,13} drive. The highly nonlinear, turbulent regime of RT instability was studied mostly in the classical regime.^{8–11} Weakly nonlinear features, such as harmonic generation and mode coupling to longer wavelengths, were measured in experiments using indirect drive^{12,19} coupled to targets with preimposed, single-mode, and multimode initial perturbations. The saturation amplitudes of 3-D broadband nonuniformities were measured using laser-imprinted modulations as initial seeds for RT growth (conditions most relevant to direct-drive ICF).¹⁸ In those experiments, the finite target thickness limited unstable hydrodynamic growth, which did not allow accurate measurements of the nonlinear velocities.²⁰ The experiments in this article present the first measurements of nonlinear saturation velocities, allowing a direct comparison with the Haan nonlinear-growth model²¹ near saturation levels. The transition from linear to nonlinear growth of 3-D broadband modulations presented in this article is among the key factors required to

understand nonlinear RT instability. This experimental study is critical to the success of ICF because most ICF ignition designs rely on the accuracy of Haan’s predictions.

Experimental Details

In the experiments, initially smooth, 1-mm-diam, 20- and 50- μm -thick CH targets were driven with 12-ns square pulses at a laser intensity of $\sim 5 \times 10^{13}$ W/cm² on the OMEGA Laser System.²² The modulation growth was measured with through-foil, x-ray radiography²⁰ using x rays from three different backlighters: an ~ 1.3 -keV uranium backlighter for 20- μm -thick targets and an ~ 2.0 -keV dysprosium and an ~ 2.5 -keV tantalum for 50- μm -thick targets. Harder x rays were used at later times when target modulations reached larger amplitudes. The backlighter x rays were imaged by an 8- μm pinhole array onto a framing camera, allowing for up to eight images with a temporal resolution of ~ 80 ps and a spatial resolution of ~ 10 μm to be captured at different times in each shot.²⁰ The initial target modulations, used for RT growth measurements, were imprinted by laser-intensity nonuniformities of the imprint beam, which arrived ~ 200 ps before all other drive beams, used for target acceleration.^{18,20} The process of laser imprinting takes ~ 200 ps. During this time, a plasma develops (from laser ablation) between the laser absorption (near the critical surface) and ablation surfaces, which decouples laser beams from the target, thereby stopping the imprinting process.^{23,24} Two different initial target modulations were created by a laser beam with either a standard distributed phase plate²⁵ (SG8 DPP) or a laser beam with no DPP, defocused to an ~ 1 -mm spot. Figure 103.19 shows measured central, 333- μm -sq parts of laser equivalent-target-plane images with an SG8 DPP [Fig. 103.19(a)] and with no DPP [Fig. 103.19(b)]. The laser-modulation Fourier spectra of these laser images are shown in Fig. 103.19(c). The beam with a DPP (solid curve) has broadband modulations with spatial frequencies up to ~ 320 mm⁻¹, corresponding to the smallest spatial size of ~ 3 μm and an intensity modulation σ_{rms} of $\sim 94\%$. The beam with no DPP (dashed curve) has modulations with spatial frequencies up to ~ 50 mm⁻¹, corresponding to the smallest spatial size of ~ 20 μm , and an intensity modulation σ_{rms} of $\sim 51\%$.

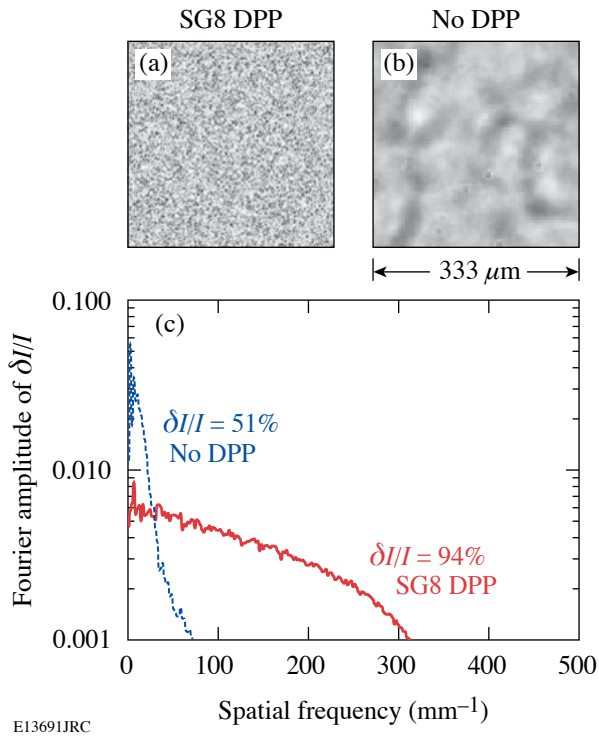


Figure 103.19 Central, 333- μm -sq parts of the measured equivalent-target-plane images of laser beams with (a) a regular SG8 DPP and (b) with no DPP used to produce initial 3-D broadband modulations for RT growth. (c) Fourier amplitudes of relative laser intensity as a function of a spatial frequency of these laser-beam images with a SG8 DPP (solid line) and with no DPP (dashed line).

Experimental Results

The optical-depth (OD) images (obtained by taking the natural logarithm of intensity-converted, framing-camera images) of x-ray radiographs are shown in Figs. 103.20(a), 103.20(b), and 103.20(c) for SG8 DPP initial conditions and in Figs. 103.20(d), 103.20(e), and 103.20(f) for no-DPP initial conditions. The early-time images (a) and (d) were obtained using a uranium backlighter, while later-time images (b) and (e) were obtained with a dysprosium backlighter and images (c) and (f) with a tantalum backlighter. A Wiener filter (based on measured system resolution and noise) was applied to these images to remove noise and deconvolve the system's modulation transfer function to recover target OD modulations.²⁰ The measured target OD variations are proportional to the variations of target areal density $\delta[\rho R]$, $\delta[\text{OD}(t)] = \mu_{\text{CH}}(E)\delta[\rho R(t)]$, where $\mu_{\text{CH}}(E)$ is the CH target mass absorption rate at the x-ray energy E used for backlighting and t is the time of the measurement. The measured (in undriven targets) mass absorption rates were $950 \pm 100 \text{ cm}^2/\text{g}$, $320 \pm 30 \text{ cm}^2/\text{g}$, and $240 \pm 20 \text{ cm}^2/\text{g}$ for uranium, dysprosium, and tantalum backlighters, respectively. The

areal-density modulations were obtained by dividing measured OD modulations by the target mass absorption rates. Harder x rays were used to measure higher-amplitude modulations at late times because softer x rays are completely absorbed in large modulation spikes, compromising the measurements. Measurement timings of 20- μm -thick targets were converted to those of 50- μm -thick targets according to the calculated (by 1-D hydrocode *LILAC*²⁶) target distance traveled.

During the acceleration phase, the target's laser-imprinted modulations grow because of RT instability. During this growth, the modulations shift to longer wavelengths, with initial small structures growing into large bubbles (the dark regions in x-ray radiographs shown in Fig. 103.20) and narrow spikes (light areas in the radiographs). Figure 103.21 shows the evolution of modulation areal-density Fourier amplitudes (for shots with DPP initial seeds). The dotted line is the Haan saturation level²⁰ $S_k = 2/Lk^2$, where $L = 333 \mu\text{m}$ is the box size of the x-ray image, k is the spatial wave number of modulations, $k = 2\pi f$, and f is the spatial frequency. The saturation level S_k was converted to areal density by multiplying it by the *LILAC*-calculated foil density of $\sim 1.7 \text{ g/cc}$, which was predicted to be constant (within about 10%) for the duration of the experiment. In the Haan model,²¹ the spectral amplitudes grow exponentially with the RT growth rate $\gamma(k)$ until they reach the saturation levels S_k ; at this point they grow

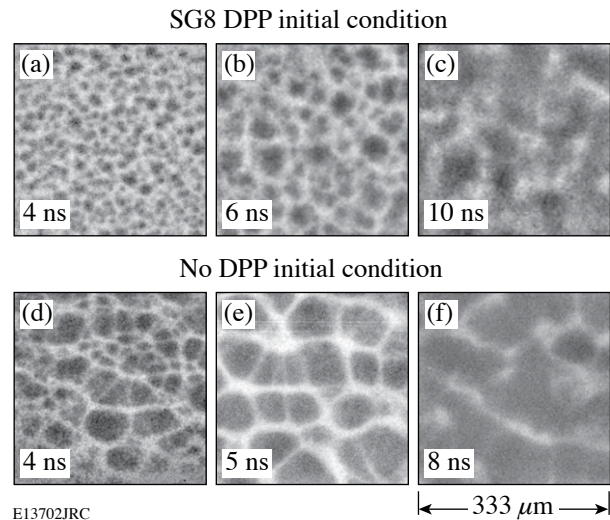


Figure 103.20 X-ray radiographs of the 3-D broadband modulations initially produced by the imprinting of the laser beam with a SG8 DPP and measured at 4, 6, and 10 ns [images (a), (b), and (c), respectively] and with the laser beam with no DPP and measured at 4, 5, and 8 ns [images (d), (e), and (f), respectively].

linearly in time with saturation velocities $V_s(k) = S_k \gamma(k)$. The RT growth rate is determined by the Betti–Goncharov dispersion relation²⁷ $\gamma(k) = 0.94 [\text{kg}/1 + kL_m]^{0.5} - 1.5kV_a$, where $g = 10 \mu\text{m}/\text{ns}^2$ is the target acceleration, $V_a = 0.65 \mu\text{m}/\text{ns}$ is the ablation velocity, and $L_m = 0.1 \mu\text{m}$ is the density scale length (all three parameters were calculated by *LILAC*). The shorter-wavelength modes grow most rapidly and quickly saturate at levels S_k while the longer-wavelength modes grow more slowly. As a result, the mid-wavelength modes have the largest growth factors, producing a peak in the spectrum. As the evolution continues, this peak moves to longer wavelengths, as shown in Fig. 103.21. Because the effects of finite target thickness, which compromised the evolution of the thin, 20- μm -thick targets in previous experiments,²⁰ were detected only after ~ 7 ns in the present experiments with 50- μm -thick targets, the analysis was limited to data taken up to ~ 6 ns.

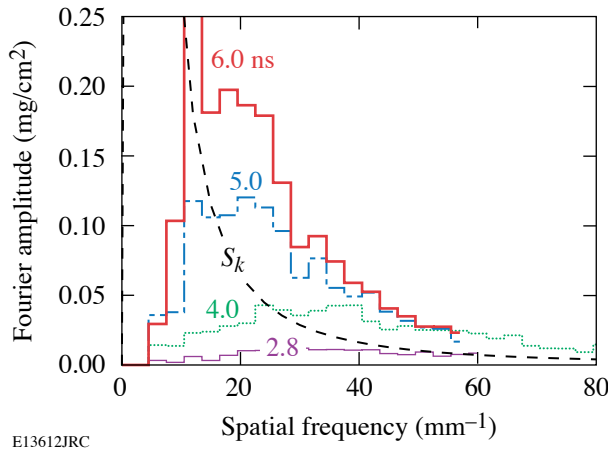


Figure 103.21
Fourier amplitudes of the target areal-density modulations as a function of spatial frequency initially produced by the imprinting of the laser beam with SG8 DPP and measured at 2.8 (thin solid), 4.0 (dotted), 5.0 (dotted-dashed), and 6.0 ns (thick solid curve). The dashed curve corresponds to the saturation amplitude predicted by Haan.²⁰

Figure 103.22 shows the temporal evolution of the areal-density Fourier amplitudes at four spatial wavelengths of 20, 30, 60, and 120 μm for shots with DPP initial conditions. The amplitudes of the 120- μm spatial wavelength [see Fig. 103.22(a)] are below their saturation levels S_k . They are growing exponentially in the linear regime. The solid lines in Figs. 103.22(a) and 103.22(b) are the exponential fits to the data, from which the growth rate is determined. The amplitudes of the 60- μm -wavelength modulations [see Fig. 103.22(b)] undergo a transition from exponential growth to linear temporal growth. The solid lines represent the exponential fit to the data below the saturation level S_k , while the dashed lines represent

the linear fit above the saturation level. The dotted lines in Figs. 103.22(c) and 103.22(d) are the linear fits to the 30- and 20- μm -wavelength data above their saturation levels. Similar fits were performed to the data with no DPP initial conditions. Figure 103.23 summarizes the growth results. The dashed line in Fig. 103.23(a) shows the growth rate $\gamma(k)$ (defined in the previous paragraph) as a function of spatial frequency. The diamonds correspond to the measured growth rates of 120- and 60- μm -wavelength modulations (corresponding to the spatial frequencies of 8 and 16 mm^{-1} , respectively) from all shots (with initial conditions including both SG8 DPP and no DPP). The dashed line in Fig. 103.23(b) shows the saturation velocity $V_s(k) = S_k \gamma(k)$ as a function of the spatial frequency, as defined by the Haan model.²¹ The diamonds correspond to the measured saturation velocities of the 120-, 60-, 30-, and 20- μm -wavelength modulations (corresponding to spatial frequencies of 8, 16, 33, and 50 mm^{-1} , respectively). The measured saturation velocities are in excellent agreement with Haan-model²¹ predictions. Once the modulations enter the nonlinear regime, the velocities no longer depend on initial conditions. The measured growth rates of long-wavelength modulations are higher (by about a factor of 2) than the Haan-model predictions (given by the Betti–Goncharov formula). Previous studies^{28,29} have predicted enhanced growth (with respect to the Haan model) of long-wavelength modes in the classical RT instability (without

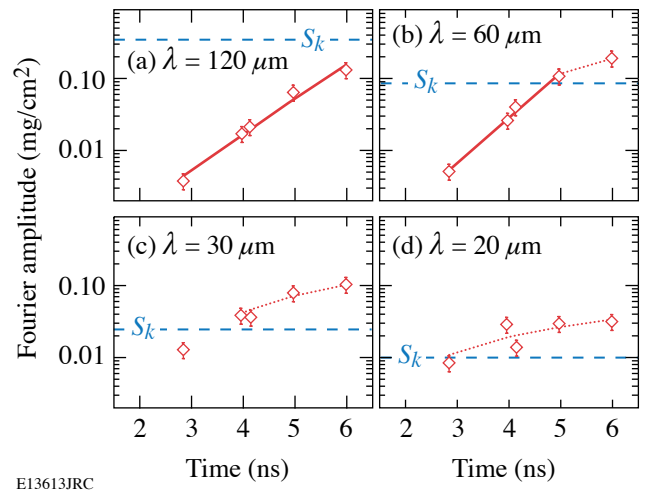


Figure 103.22
Temporal evolution of the target areal-density modulations measured at spatial wavelengths of 120, 60, 30, and 20 μm [(a), (b), (c), and (d), respectively]. The solid and dotted lines represent exponential and linear-in-time fits to the experimental data, respectively, initially produced by the imprinting of the laser beam with an SG8 DPP. The horizontal dashed lines show the saturation amplitudes predicted by Haan.²⁰

ablation stabilization) because of enhanced mode-coupling of higher-amplitude, faster-growing, shorter-wavelength modes. The same studies,^{28,29} however, predicted no significant contribution of mode coupling for the ablative RT growth (relevant to our experiments). A recent study³⁰ by Sanz *et al.* predicted enhanced mode coupling to longer-wavelength modes in the ablative RT instability, compared to the classical RT case. The present experiments are consistent with this new study³⁰ rather than with the previous predictions.^{28,29} This correction to the Haan model has a small effect on the overall growth of the total rms modulation level because the longer wavelengths (120 μm and 60 μm) have smaller amplitudes than the shorter-wavelength modes (as shown in Fig. 103.21) and shorter modes grow with the velocities that are in agreement with Haan model. Therefore, the average modulation levels (rms amplitudes) grow very close to Haan-model predictions.²¹ We find it remarkable that this simple model predicts so accurately such a complicated phenomenon as the nonlinear saturation of the RT instability.

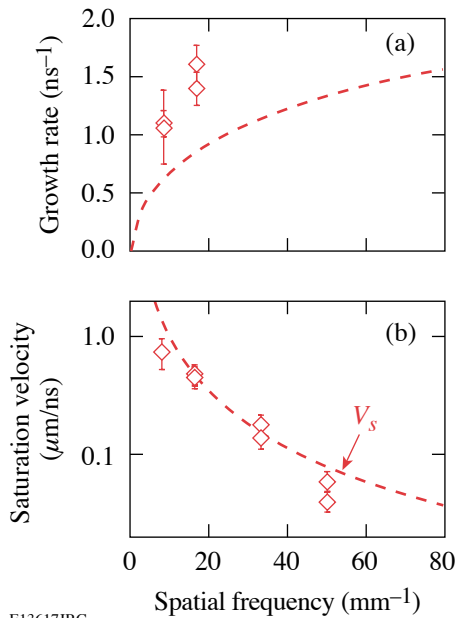


Figure 103.23

(a) Modulation RT growth rates as a function of spatial frequency measured (diamonds) and predicted by the Betti–Goncharov dispersion relation (dashed curve). (b) Modulation nonlinear saturation velocities as a function of spatial frequency measured (diamonds) and predicted by the Haan model (dashed curve).

Figure 103.24 shows the evolution of power spectra at three different times (with no DPP initial conditions). In the highly nonlinear, turbulent regime, it has been determined that the power spectra follow the “ $-5/3$ ” Kolmogorov power-law scaling.¹⁰ In the present experiments, the modulations undergo the

transition from linear to nonlinear growth near the saturation levels. At a later time (~ 5.9 ns), a large part of the modulation spectrum is in the nonlinear regime, while modulations at 2.5 and 3.8 ns approach the saturation levels. The thin, solid line presents the power-law fit to the 5.9-ns data showing the power-law slope of ~ -2.1 . This slope is steeper than Kolmogorov’s slope of $-5/3 = -1.67$, shown by a dotted line. Once the modulations enter the highly nonlinear, turbulent regime of RT instability, the slope is expected to approach $-5/3$, as was shown in earlier classical RT experiments.¹¹

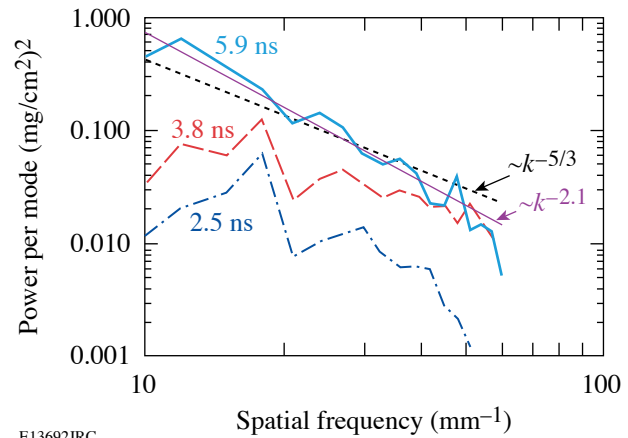


Figure 103.24

Measured power per mode of areal-density modulations at 2.5, 3.8, and 5.9 ns. The thin and dashed curves represent the lines with power-law slopes of -2.1 and -1.67 (or $-5/3$), respectively.

Conclusions

In conclusion, the unstable RT growth of 3-D broadband modulations was measured near nonlinear saturation levels in planar plastic targets directly accelerated by laser light. The nonlinear saturation velocities were measured for the first time and are in excellent agreement with the Haan model.²¹ Once modulations enter the nonlinear regime, the measured growth does not depend on the initial modulation spectrum. The measured growth of low-amplitude, long-wavelength modes is consistent with the generation of enhanced nonlinear long wavelengths in ablatively driven targets, predicted³⁰ by Sanz *et al.* This experimental study is critical to the success of ICF because most ICF ignition designs rely on Haan’s predictions.

ACKNOWLEDGMENT

The authors thank Prof. D. Shvarts, Prof. R. Betti, and Dr. B. A. Remington for helpful discussions. This work was supported by the U.S. Department of Energy Office of Inertial Confinement Fusion under Cooperative Agreement No. DE-FC52-92SF19460, the University of Rochester, and the New York State Energy Research and Development Authority. The support

of DOE does not constitute an endorsement by DOE of the views expressed in this article.

REFERENCES

1. J. Nuckolls *et al.*, *Nature* **239**, 139 (1972).
2. B. A. Remington *et al.*, *Phys. Plasmas* **4**, 1994 (1997).
3. S. E. Bodner, D. G. Colombant, J. H. Gardner, R. H. Lehmborg, S. P. Obenschain, L. Phillips, A. J. Schmitt, J. D. Sethian, R. L. McCrory, W. Seka, C. P. Verdon, J. P. Knauer, B. B. Afeyan, and H. T. Powell, *Phys. Plasmas* **5**, 1901 (1998).
4. J. D. Lindl, *Phys. Plasmas* **2**, 3933 (1995).
5. G. Dimonte and B. Remington, *Phys. Rev. Lett.* **70**, 1806 (1993).
6. Y. Aglitskiy *et al.*, *Phys. Plasmas* **9**, 2264 (2002).
7. J. W. Jacobs and V. V. Krivets, *Phys. Fluids* **17**, 034105 (2005).
8. O. Sadot *et al.*, *Phys. Rev. Lett.* **80**, 1654 (1998).
9. K. I. Read, *Physica* **12D**, 45 (1984).
10. M. B. Schneider, G. Dimonte, and B. Remington, *Phys. Rev. Lett.* **80**, 3507 (1998).
11. G. Dimonte *et al.*, *Phys. Fluids* **16**, 1668 (2004).
12. B. A. Remington *et al.*, *Phys. Fluids B* **5**, 2589 (1993).
13. K. S. Budil *et al.*, *Phys. Rev. Lett.* **76**, 4536 (1996).
14. K. Shigemori *et al.*, *Phys. Rev. Lett.* **78**, 250 (1997).
15. C. J. Pawley *et al.*, *Phys. Plasmas* **4**, 1969 (1997).
16. J. P. Knauer, R. Betti, D. K. Bradley, T. R. Boehly, T. J. B. Collins, V. N. Goncharov, P. W. McKenty, D. D. Meyerhofer, V. A. Smalyuk, C. P. Verdon, S. G. Glendinning, D. H. Kalantar, and R. G. Watt, *Phys. Plasmas* **7**, 338 (2000).
17. T. Sakaiya *et al.*, *Phys. Rev. Lett.* **88**, 145003 (2002).
18. V. A. Smalyuk, T. R. Boehly, D. K. Bradley, V. N. Goncharov, J. A. Delettrez, J. P. Knauer, D. D. Meyerhofer, D. Oron, and D. Shvarts, *Phys. Rev. Lett.* **81**, 5342 (1998).
19. M. M. Marinak *et al.*, *Phys. Rev. Lett.* **80**, 4426 (1998).
20. V. A. Smalyuk, T. R. Boehly, D. K. Bradley, V. N. Goncharov, J. A. Delettrez, J. P. Knauer, D. D. Meyerhofer, D. Oron, D. Shvarts, Y. Srebro, and R. P. J. Town, *Phys. Plasmas* **6**, 4022 (1999).
21. S. W. Haan, *Phys. Rev. A, Gen. Phys.* **39**, 5812 (1989).
22. T. R. Boehly, D. L. Brown, R. S. Craxton, R. L. Keck, J. P. Knauer, J. H. Kelly, T. J. Kessler, S. A. Kumpan, S. J. Loucks, S. A. Letzring, F. J. Marshall, R. L. McCrory, S. F. B. Morse, W. Seka, J. M. Soures, and C. P. Verdon, *Opt. Commun.* **133**, 495 (1997).
23. S. E. Bodner, *J. Fusion Energy* **1**, 221 (1981).
24. V. N. Goncharov, S. Skupsky, T. R. Boehly, J. P. Knauer, P. McKenty, V. A. Smalyuk, R. P. J. Town, O. V. Gotchev, R. Betti, and D. D. Meyerhofer, *Phys. Plasmas* **7**, 2062 (2000).
25. Y. Lin, T. J. Kessler, and G. N. Lawrence, *Opt. Lett.* **20**, 764 (1995).
26. J. Delettrez, R. Epstein, M. C. Richardson, P. A. Jaanimagi, and B. L. Henke, *Phys. Rev. A, Gen. Phys.* **36**, 3926 (1987).
27. R. Betti, V. N. Goncharov, R. L. McCrory, and C. P. Verdon, *Phys. Plasmas* **5**, 1446 (1998).
28. S. W. Haan, *Phys. Fluids B* **3**, 2349 (1991).
29. D. Ofer, U. Alon, D. Shvarts, R. L. McCrory, and C. P. Verdon, *Phys. Plasmas* **3**, 3073 (1996).
30. J. Sanz, J. Ramírez, R. Ramis, R. Betti, and R. P. J. Town, *Phys. Rev. Lett.* **89**, 195002 (2002).